Thermal conduction properties of Mo/Si multilayers for extreme ultraviolet optics

Elah Bozorg-Grayeli, Zijian Li, Mehdi Asheghi, Gil Delgado, Alexander Pokrovsky et al.

Citation: J. Appl. Phys. **112**, 083504 (2012); doi: 10.1063/1.4759450
View online: http://dx.doi.org/10.1063/1.4759450
View Table of Contents: http://jap.aip.org/resource/1/JAPIAU/v112/i8
Published by the American Institute of Physics.

Thermal conduction properties of Mo/Si multilayers for extreme ultraviolet optics

Elah Bozorg-Grayeli,[1,a)] Zijian Li,[1] Mehdi Asheghi,[1] Gil Delgado,[2] Alexander Pokrovsky,[2] Matthew Panzer,[2] Daniel Wack,[2] and Kenneth E. Goodson[1]
[1]*Department of Mechanical Engineering, Stanford University, Stanford, California 94305, USA*
[2]*KLA-Tencor Corporation, 1 Technology Drive, Milpitas, California 95035, USA*

(Received 20 July 2012; accepted 25 September 2012; published online 16 October 2012)

Extreme ultraviolet (EUV) lithography requires nanostructured optical components, whose reliability can be influenced by radiation absorption and thermal conduction. Thermal conduction analysis is complicated by sub-continuum electron and phonon transport and the lack of thermal property data. This paper measures and interprets thermal property data, and their evolution due to heating exposure, for Mo/Si EUV mirrors with 6.9 nm period and Mo/Si thickness ratios of 0.4/0.6 and 0.6/0.4. We use time-domain thermoreflectance and the 3ω method to estimate the thermal resistance between the Ru capping layer and the Mo/Si multilayers ($R_{Ru\text{-}Mo/Si} = 1.5$ m^2 K GW^{-1}), as well as the out-of-plane thermal conductivity ($k_{Mo/Si}$ 1.1 W m^{-1} K^{-1}) and thermal anisotropy ($\eta = 13$). This work also reports the impact of annealing on thermal conduction in a co-deposited $MoSi_2$ layer, increasing the thermal conductivity from 1.7 W m^{-1} K^{-1} in the amorphous phase to 2.8 W m^{-1} K^{-1} in the crystalline phase. © *2012 American Institute of Physics*. [http://dx.doi.org/10.1063/1.4759450]

I. INTRODUCTION

Extreme ultraviolet lithography (EUVL) is a promising technique for scaling microelectronic devices beyond the 22 nm node.[1,2] The wavelength of the optical radiation used (~13.5 nm) significantly improves the diffraction-limited resolution with respect to lithographic techniques in the deep-UV range. Few materials or material combinations are capable of reflecting such EUV wavelengths, and optics lifetime is challenging. Mirrors must withstand photon energies on the order of 90 eV, which is substantially larger than the ionization energies of many of the materials used for optical components (e.g., 34 eV/particle for the third Si ionization energy). Periodic multilayers offer a way to circumvent these issues. Unlike single-material mirrors, these structures consist of multiple bilayers of materials with varying indices of refraction.[3] By carefully controlling the material properties and thicknesses, one can use constructive interference to create highly reflective surfaces at a given wavelength.[4,5] In the case of EUV wavelengths, such stacks consist of ~6 nm bilayers composed of alternating layers of molybdenum and amorphous silicon.

While much previous research has been published on the optical performance of Mo/Si-coated masks and mirrors,[1–4,6] there is currently no rigorous information about their thermal properties and temperature fields resulting from radiation absorption. Considering that many experiments demonstrated that damage can occur in these materials due to long-term/high-temperature radiation exposure,[7–9] a detailed understanding of their thermal properties is appropriate at this time. However, nanoscale thermal transport effects in the Mo/Si multilayer stack complicate this task. Interface scattering within the mirror structure significantly reduces the mean free path (MFP) of the thermal energy carriers. This reduces the film thermal conductivity below what we expect for bulk Mo and a-Si. Further, interface scattering affects cross-plane MFP considerably more than in-plane, which can result in very significant thermal conductivity anisotropy. Lastly, although thermal conduction in bulk Mo is electron-dominated, the low thickness of the Mo film and the presence of the dielectric a-Si layers restrict the electron mean free path, changing the relative contributions of electrons and phonons to heat conduction, particularly in the through-plane direction.[10] These factors impede thermal conduction through the Mo/Si stacks, resulting in higher operating temperatures. This can increase the risk of degradation in mirror reflectivity.

During fabrication of the Mo/Si multilayer, a thin layer of a-$MoSi_2$ forms at each interface.[7] Over the lifetime of the material, constant exposure to elevated temperatures will cause this layer to crystallize,[8] after which Mo and Si will interdiffuse further.[7–9] Mirror temperature governs the rate of diffusion, given by[3,8]

$$D = D_0 \exp\left(-\frac{E_\alpha}{k_B T}\right), \tag{1}$$

where D_0 is the temperature-independent interdiffusion coefficient, E_α is the interdiffusion activation energy, and k_B is Boltzmann's constant. The thickness of the interdiffused region increases with time, given by[8]

$$w^2(t) = 2Dt + w^2(0), \tag{2}$$

where w is the thickness of the interdiffused region and t is time. During this process, the higher-density c-$MoSi_2$ film consumes the lower-density a-Si layer, reducing the periodicity of the stack and altering its optical properties. The

[a)]Electronic mail: ebozorgg@stanford.edu.

required lifetime therefore limits the allowed operating temperature of the device. The thermal properties of the mirror, in turn, limit the influence that can be tolerated while keeping the peak temperature below this threshold.

This work measures the thermal properties of thin film mirror materials for use in simulations and reliability predictions for EUV mirrors. In addition to measuring the thermal properties of the multilayer Mo/Si stack, we also report the thermal conductivities and boundary resistances offered by the capping and absorber layers on the mirror surface. To accomplish this, we apply both picosecond time-domain thermoreflectance (TDTR) and frequency-domain electrical thermometry (the 3ω method) with bridges of varying width down to 50 nm on a variety of thin film samples, including (1) the multilayer Mo/Si stack, (2) the interdiffused $MoSi_2$ region, (3) the TaN absorber film, and (4) the Ru capping layer. The final section of this manuscript assesses the impact of the measured properties on the total thermal resistance and temperature rise experienced at an EUV spot on a mirror structure.

II. SAMPLE DESIGN

A. Mirror/mask structure

The multilayer mirror/mask structure consists of four separate parts: substrate, multilayer, capping layer, and absorber (Fig. 1). The structure is then coated with additional metal and dielectric layers as required by the specific measurement technique. The substrate acts as a mechanical support and provides a heat diffusion path from the multilayer to the heat sink. In a mirror application, low thermal expansion materials such as quartz serve as the substrate. However, to improve heat diffusion from the multilayer during measurement, we substituted silicon.

The multilayer mirror stack sits directly on the substrate. The complete mirror structure consists of a 6.9 nm/bilayer stack (Fig. 2). Each period contains 2.2 nm of a-Si, 2.6 nm of Poly-Mo, and 2.0 nm of interdiffused a-$MoSi_2$. The thickness of the interdiffused layer varies depending on the temperature history of the multilayer and whether the surface was a-Si deposited on Poly-Mo (0.7 nm) or vice versa (1.3 nm). Several papers have noted the variation in interdiffusion layer thickness.[7–9,11] Zubarev argued that the crystalline nature of the Mo film makes it difficult for silicon atoms to diffuse in during deposition.[9] However, as Mo is deposited, the covalent bonds in the a-Si layer are easily broken, resulting in a thicker a-$MoSi_2$ layer.

Since the Mo/Si multilayer structure is not stable in air, a Ru capping layer coats the multilayer mirror material.[12] The purpose of this layer is to minimize oxidation in the mirror material without adversely affecting the stress profile or reflectivity in the multilayer.[6,13,14] Yan *et al.* demonstrated that a 2 nm Ru layer maximizes the reflectivity of the stack while offering protection against oxidation.[14] The last film in the EUV mask stack is the absorber. This film must be capable of absorbing electromagnetic radiation in the range of extreme UV to soft x-rays. Further, it must not exert undue stress upon the rest of the mirror structure. Au, W, Ta, and TaN are common absorber film selections.[15,16] TaN offers low stress,[16] an amorphous/poly-crystalline structure,[16–18] and good absorption properties in EUV.[16]

The complete mirror structure is more complex—and therefore poses greater challenges for minimizing the uncertainty—than many structures measured using both picosecond TDTR and the 3ω method. In order to accurately model the thermal resistance experienced by an EUV pulse, we must account for the thermal resistances of the TaN absorber, the Ru capping layer, and the Mo/Si multilayer stack. This becomes even more complex when one accounts for the thermal boundary resistances (TBR) between the Ru capping layer and the Mo/Si mirror, and the impact of the a-$MoSi_2$ interdiffused region. To address these tasks, we designed several simpler structures to mimic the individual films, interfaces, and interdiffused regions within the EUVL mask structure.

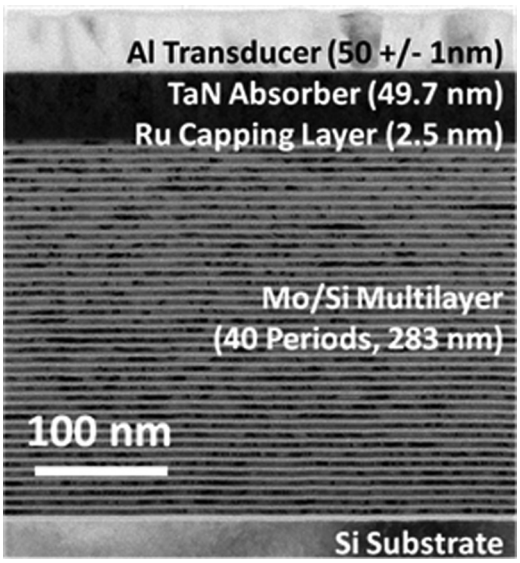

FIG. 1. Cross-sectional view of a Mo/Si-based mirror, consisting of substrate, multilayers, capping layer, and absorber. The additional Al transducer layer was added for optical thermoreflectance measurements.

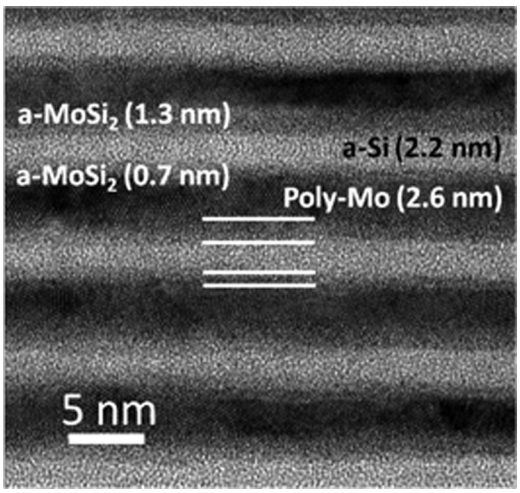

FIG. 2. Cross-sectional view of a Mo/Si bilayer mirror structure. The white lines in the center indicate (top-down) the Poly-Mo/a-$MoSi_2$, a-$MoSi_2$/a-Si, a-Si/a-$MoSi_2$, and a-$MoSi_2$/Poly-Mo interfaces.

B. Single film TaN

We prepared three samples of varying TaN thickness: 50 nm, 75 nm, and 100 nm. Half of each sample was coated with 50 nm Al for optical measurements, while the remaining half was left uncovered for electrical sheet resistance measurements. Although TEM images and nanobeam diffraction data show the morphology of the films to be the same, electrical measurements demonstrated thickness-dependent electrical resistivity.[18]

C. Multilayer Mo/Si

In order to understand the thermal behavior of the Mo/Si multilayer stack, we must extract three critical thermal properties: cross plane thermal conductivity, in-plane thermal conductivity, and the thermal resistance contribution of the capping layer. We therefore fabricated samples containing 20 periods of Mo/Si on silicon. Half of the samples were left uncapped for 3ω measurements of cross-plane and in-plane thermal conductivity. The remaining samples received 50 nm coatings of Al or Ru for optical thermoreflectance measurements. Both materials are excellent thermoreflectance transducers,[19] and allow direct measurement of the Ru-Mo/Si and Al-Mo/Si TBRs. We selected two Mo/Si ratios for measurement: 0.4/0.6 and 0.6/0.4. In both cases, the total thickness of each bilayer remained 6.9 nm.

D. Single film $MoSi_2$

The $MoSi_2$ samples were prepared by co-sputtering Mo and Si onto a Si wafer at 300 K. The targeted sample thicknesses were 100, 200, and 250 nm. The thicknesses were chosen to avoid size effect issues in measuring thermal conductivity. Since these films were co-sputtered at room temperature, the $MoSi_2$ layers were amorphous. Subsequently, we deposited a 50 nm Al transducer layer on half of the $MoSi_2$ wafer for thermoreflectance measurements. The other half was left uncoated for electrical conductivity measurements.

III. EXPERIMENTAL METHODS

Many techniques exist to extract thermal properties at nanometer length scales. Such methods rely on measuring the temperature response of a material to heat input. These methods achieve high thermal resistance resolutions by confining their heat inputs either temporally or spatially. Examples of temporal confinement techniques include time-domain thermoreflectance[20,21] and the 3ω technique.[22] In these examples, a heating pulse or high-frequency heating signal confines the measured region to the thermal penetration depth of the sample. This depth is defined by

$$d_{thermal} = \sqrt{\alpha\tau}, \tag{3}$$

where α is the thermal diffusivity of the heated film, and τ is the characteristic time of the heating event. For a heating event, this could be roughly defined as the full-width half maximum (FWHM) of the pulse. For a high-frequency measurement, τ is defined as the heating period. Spatial confinement, on the other hand, restricts the depth of heating by using varying widths of heater structures. Examples of this include steady-state electrical thermometry measurements[23,24] based on structures similar to the 3ω technique. Spatial confinement also allows one to extract in-plane thermal properties without the use of a suspended structure.[25] These techniques are grouped into the more general categories of optical and electrical thermometry. In this section, we describe the methods used in our study.

A. Optical heating and thermometry

Picosecond TDTR is an optical pump-probe technique which uses an ultrafast laser system as a simultaneous heat source and thermometer.[26,27] In this measurement, a passively modelocked Nd:YVO_4 laser generates 9.2 ps optical pulses at 1064 nm. A half waveplate and polarizing beamsplitter separate this pulse into pump and probe components, with the pump intensity being significantly greater than the probe. The pump beam travels along a fixed optical path, during which it is frequency-doubled and modulated by an electro-optic modulator. The pump then travels through an objective and heats a metal transducer on the sample with a 10 μm-wide Gaussian beam. The probe beam travels along a separate optical path containing a linear delay stage. This stage controls the total path length taken by the probe beam, allowing us to control the relative delay between when pump and probe strike the sample. Using a lock-in amplifier, we measure the reflected probe signal component at the pump modulation frequency. This reflected signal scales linearly with the transducer temperature,[20,28] allowing us to construct a plot of normalized transducer temperature as a function of time after the heating event (Fig. 3). Using a theoretical model of heat diffusion through a multilayer stack of materials due to modulated optical heating,[21,29] we extract the thermal properties of the films beneath the transducer. By using an optical access oven, we extend these measurements to temperatures on the order of 700 K.[27,30]

B. Electrical heating and thermometry

Frequency-domain electrical thermometry, known as the 3ω technique,[22] measures the two-dimensional thermal conductivity of a Mo/Si multilayer sample. The metal patterns

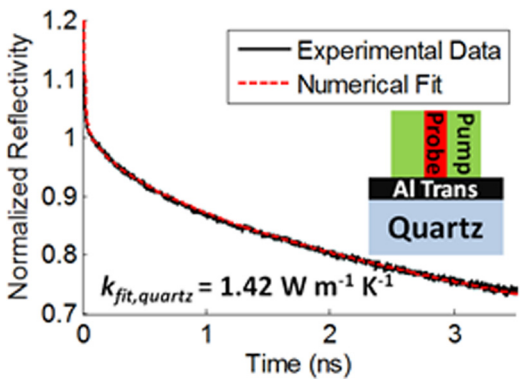

FIG. 3. Characteristic thermal decay trace for picosecond TDTR measurement of a 50 nm Al transducer on quartz. The numerical fit corresponds to a quartz thermal conductivity of 1.42 W m^{-1} K^{-1}.

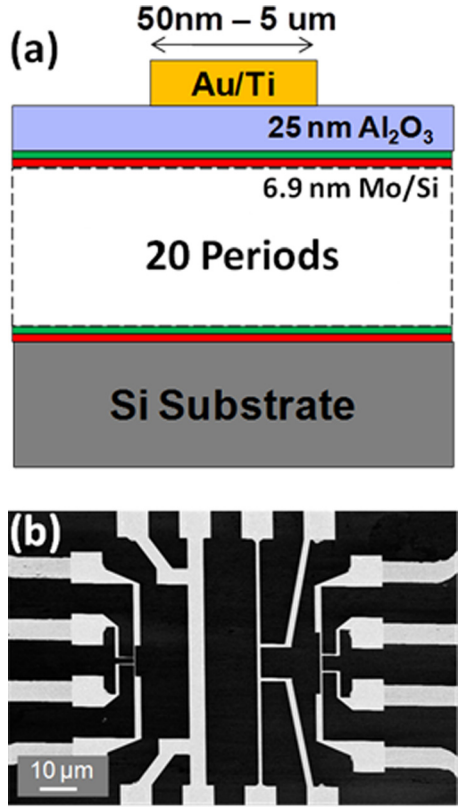

FIG. 4. Patterned heater bridges for electrical thermometry. (a) Sample schematic. The 25 Al_2O_3 layer provides insulation between the heater bridge and the Mo/Si multilayer. (b) Scanning electron microscope image of the patterned heater bridges with widths varying from 50 nm to 5 μm (not all widths are shown in this micrograph).

consist of 5 nm of titanium as an adhesion layer and 55 nm of gold as heater bridges. Electron-beam lithography fabricates the fine structures of the heaters with line widths varying from 50 nm to 5 μm (Fig. 4). When an ac current with frequency ω flows through the heater bridge, the voltage signal across it contains a 3rd harmonic (3ω) component due to Joule heating and the linear relationship between temperature and electrical resistivity of the metal heater. The amplitude of the 3ω component contains information of the thermal conductivity of underlying materials. Wide heaters (5 μm) generate nearly one-dimensional heat conduction through the multilayer stack, which are sensitive to the out-of-plane thermal conductivity. Narrow heaters (50 nm) induce two-dimensional heat transfer within a shallow region near the top, and capture the in-plane thermal conductivity. A recursive matrix formulation, developed by Kim *et al.*,[31] extracts the thermal conductivity and anisotropy of each layer. Since the Mo/Si multilayer stack is conductive with an electrical conductivity of $1.86 \times 10^6\ \Omega^{-1}\ m^{-1}$, we deposit an amorphous Al_2O_3 layer on the top to provide electrical insulation. We also prepare a reference sample with identical structures absent the Mo/Si multilayers. The reference sample facilitates the separation of the contribution of Mo/Si multilayers to the measured total thermal resistance. The electrical measurements are performed at room temperature to minimize the interdiffusion between Mo and Si layers.

IV. RESULTS AND DISCUSSION

The TaN and $MoSi_2$ samples were measured for a temperature range of 300 K to 700 K. Since the Mo/Si films are prone to interdiffusion at elevated temperatures, these samples were restricted to room temperature measurements. Table I reports a summary of the room temperature thermal property data obtained using TDTR and 3ω methods. The TaN data from Bozorg-Grayeli *et al.*[18] are also reported here.

Picosecond TDTR and 3ω measurements extracted the cross-plane thermal conductivity of the $Mo_{0.4}/Si_{0.6}$ multilayer, respectively, as $1.1 \pm 0.1\ W\ m^{-1}\ K^{-1}$ to $1.2 \pm 0.07\ W\ m^{-1}\ K^{-1}$. The cross-plane conductivity of the $Mo_{0.6}/Si_{0.4}$ sample is slightly higher at $1.4 \pm 0.1\ W\ m^{-1}\ K^{-1}$. This is due to the increased ratio of Mo, which is a more effective thermal conductor than a-Si. The recently published nonequilibrium model of Li *et al.* for phonon-electron heat conduction through Mo/Si multilayers shows similar results,[32] predicting thermal conductivities of $1.3\ W\ m^{-1}\ K^{-1}$ for $Mo_{0.4}Si_{0.6}$ and $1.49\ W\ m^{-1}\ K^{-1}$ for $Mo_{0.6}/Si_{0.4}$. Comparing the measured resistance of the bilayers to the values anticipated from bulk thermal properties, we see the effect of reduced film dimensions and TBR. Using a series resistor model with the bulk thermal properties of Mo, a-Si,[33] and the measured thermal properties of a-$MoSi_2$, $Mo_{0.4}/Si_{0.6}$ gives a conductivity $\sim 2\ W\ m^{-1}\ K^{-1}$. The thermal resistance of this ideal bilayer is $\sim 2.8\ m^2\ K\ GW^{-1}$ lower than the measured result. Applying the series resistor model with bulk Mo, a-Si, and a-$MoSi_2$ properties to the $Mo_{0.6}/Si_{0.4}$ sample, we estimate thermal conductivity $\sim 4.9\ W\ m^{-1}\ K^{-1}$. This results in a bilayer resistance $\sim 3.5\ m^2\ K\ GW^{-1}$ lower

TABLE I. Thermal properties of the components of the Mo/Si multilayer mirror system measured at 300 K using TDTR and 3ω techniques. k_{film} represents the measured thermal conductivity in the cross-plane direction. The 3ω $Mo_{0.4}/Si_{0.6}$ case notes the measured anisotropy ratio.

Sample	Technique	$R_{trans\text{-}film}$ ($m^2\ K\ GW^{-1}$)	k_{film} ($W\ m^{-1}\ K^{-1}$)	$R_{film\text{-}si}$ ($m^2\ K\ GW^{-1}$)
Al on TaN[18]	TDTR	5.5–7.6[a] (± 0.2)	3.0–3.4[b] (± 0.3)	N/A
Al on $Mo_{0.4}/Si_{0.6}$	TDTR	6.0 ± 0.2	1.1 ± 0.1	N/A
3ω	N/A	1.2 ± 0.07 ($\eta = 13 \pm 2$)	N/A	
Ru on $Mo_{0.4}/Si_{0.6}$	TDTR	1.5 ± 0.1	1.1 ± 0.1	N/A
Al on $Mo_{0.6}/Si_{0.4}$	TDTR	6.9 ± 0.3	1.4 ± 0.1	N/A
Al on a-$MoSi_2$	TDTR	5.1 ± 1.0	1.7 ± 0.2	5.3 ± 0.5
Al on c-$MoSi_2$	TDTR	5.1 ± 1.0	2.8 ± 0.3	14.5 ± 2.0

[a]Range of values is due to annealing of the interface.
[b]Range of values is due to size effects in the samples.

than the measured result. There are several potential causes for this difference. The presence of multiple nanometer-scale layers in close proximity suggest that reduced energy carrier mean free path, frequent electron-phonon energy conversion, and ballistic heat conduction may contribute to the increased thermal resistance.

Because the 3ω measurement uses heater bridges with widths of 5 μm or thinner while the TDTR setup uses a 10 μm wide pump beam, it is more sensitive to thermal spreading in the film. Using narrow heater bridges with widths of 50–100 nm, which are more sensitive to the in-plane thermal conductivity, we find the thermal conductivity anisotropy ratio $\eta = k_{in-plane}/k_{out-of-plane} = 13 \pm 2$ for $Mo_{0.4}/Si_{0.6}$. The highly anisotropic thermal conductivities of the Mo/Si multilayers confirm that the frequent interfaces significantly impede the thermal transport in the out-of-plane direction. Li *et al.* speculate that samples consisting of higher Mo ratios will not exhibit significantly different anisotropy ratios.[32]

TDTR measurements allow direct access to the transducer-film TBR. Using an Al transducer, we find the Al-Mo/Si TBR to be 6.0 ± 0.2 m^2 K GW^{-1} for $Mo_{0.4}/Si_{0.6}$ and 6.9 ± 0.3 m^2 K GW^{-1} for $Mo_{0.6}/Si_{0.4}$. Using a Ru transducer to mimic the capping layer, the transducer-Mo/Si TBR decreases to 1.5 ± 0.1 m^2 K GW^{-1}. While this value is significantly lower than the TBR caused by Al, it still greatly affects the thermal resistance offered by the 2.5 nm Ru capping layer.

Since roughly one-third of the Mo/Si multilayer stack consists of an interdiffused layer, the thermal properties of a-$MoSi_2$ contribute significantly to the properties shown above. Room temperature measurements of the in-plane electrical conductivity of a-$MoSi_2$ returned a conductivity of 1.6 mΩ^{-1} cm^{-1}. Using the Wiedemann-Franz-Lorenz (WFL) law, this translates to an expected electron thermal conductivity of 1.2 W m^{-1} K^{-1}. Further, using the $MoSi_2$ density along with minimum thermal conductivity theory,[34] we estimate a phonon thermal conductivity of 1.6 W m^{-1} K^{-1}. We obtain the high temperature thermal properties of the $MoSi_2$ films using an optical access oven pumped to vacuum. The oven was pumped down to vacuum to prevent oxidation of the transducer films. We measured $R_{Al\text{-}MoSi2}$, k_{MoSi2}, and $R_{MoSi2\text{-}Si}$ from 300 K to 700 K. Temperature ramps are performed at intervals of 100 K at a rate of 50 K/min, with a 30 min hold at each temperature. The measurement requires ~15 min for each temperature. As a result, the total measurement time was ~7 h. During this process, k_{MoSi2} increased from 1.7 W m^{-1} K^{-1} to 2.8 W m^{-1} K^{-1} (Fig. 5(a)). The increase in k_{MoSi2} was due to the crystallization of the samples (Fig. 6). Previous measurements on sputtered $MoSi_2$ thin films have shown that annealing significantly increases the electrical conductivity.[35] Chow *et al.* demonstrated a 6-fold increase in electrical conductivity after a 1-h anneal at 900 °C, attributing this change to recrystallization of the film into tetragonal $MoSi_2$.[35] Although crystallization can also increase the sound velocity and phonon mean free path relative to an amorphous film, the magnitude of the electrical conductivity change is significantly greater. As such, the majority of the thermal conductivity increase is likely due to improved electronic conduction. Subsequent high-temperature measurements of the heated films showed no change in thermal properties (Fig. 5(b)), indicating that the samples were fully crystallized. The thermal conductivity of the interdiffused film in the multilayer is likely significantly below this value due to reduced carrier mean free path.

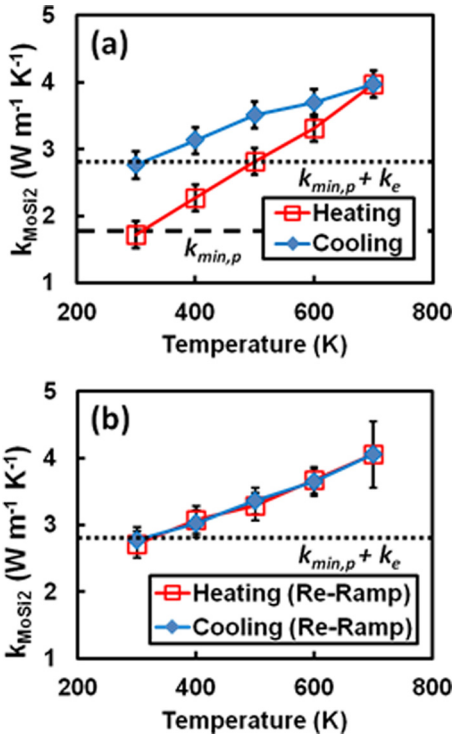

FIG. 5. Thermal conductivity of $MoSi_2$: (a) First temperature ramp and (b) subsequent re-ramp. The thermal conductivity hysteresis in (a) is due to crystallization of the $MoSi_2$ film. In (b), the film has been fully crystallized, so no hysteresis effects are visible. The dotted lines indicate the estimated thermal conductivities obtained from the minimum thermal conductivity model ($k_{min,p}$) and from WFL estimates (k_e).

The $MoSi_2$-Si TBR increases significantly during the annealing process (Fig. 7(a)), though it remains stable during subsequent high-temperature measurements (Fig. 7(b)). We propose that this is due to the presence of interfacial stresses during the initial heating, resulting in delamination at the $MoSi_2$-Si interface. Such stresses may be due to mismatch in the lattice parameters[36,37] or coefficients of thermal expansion[36,38] of the two films. The TEM images of the

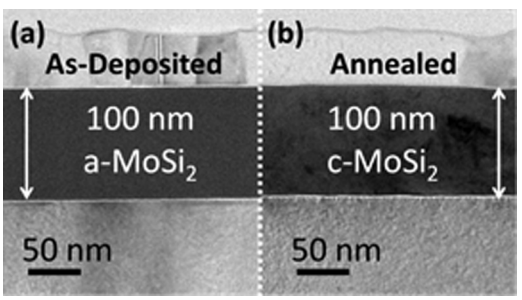

FIG. 6. Cross-sectional TEM images of the 100 nm as-deposited (a) and annealed (700 K) (b) $MoSi_2$ films, including transducer layer and substrate. We see that (a) is completely amorphous, while (b) shows crystallization. Crystallization does not change the thickness of the film.

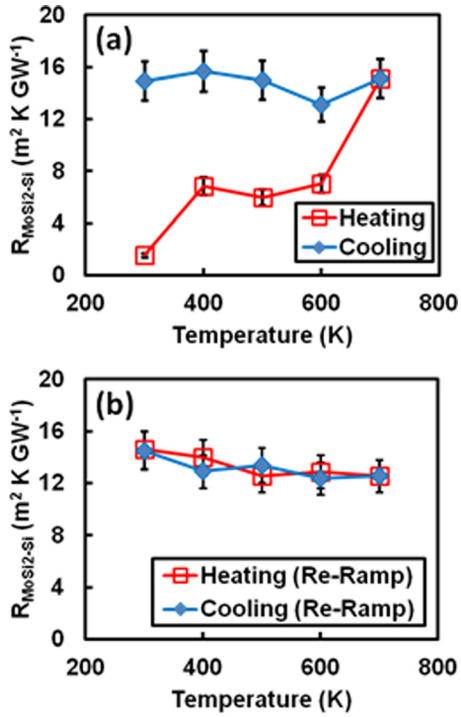

FIG. 7. Thermal boundary resistance between $MoSi_2$ and Si: (a) first temperature ramp and (b) subsequent re-ramp. The TBR hysteresis in (a) is due to heating of the $MoSi_2$ film. This process creates interface stresses, resulting in delamination. In (b), the film has been fully crystallized, and demonstrates no additional hysteresis in TBR.

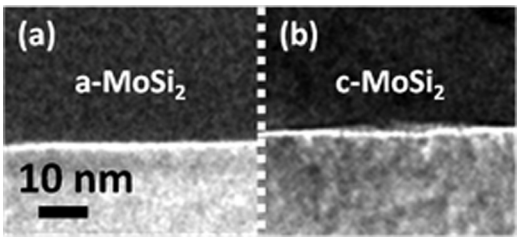

FIG. 8. Cross-sectional TEM images of the $MoSi_2$-Si interface for the (a) as-deposited and (b) annealed $MoSi_2$ films. While (a) demonstrates that the a-$MoSi_2$ conforms to the Si surface, (b) shows local deformed regions where c-$MoSi_2$ and Si do not seem to be in contact. This may be responsible for the increase in $R_{MoSi2-Si}$ upon annealing.

crystallized $MoSi_2$ seem to confirm the delamination, showing small regions at the interface where the c-$MoSi_2$ and Si do not appear to be in contact. Figure 8 compares the film-substrate interfaces for amorphous and crystalline $MoSi_2$. The a-$MoSi_2$ in Figure 8(a) conforms to the Si substrate, while the c-$MoSi_2$ in Figure 8(b) shows detachment. Although the Al-$MoSi_2$ interface becomes rougher after annealing, it does not show any delamination, nor does it demonstrate an increase in TBR. This implies that the Al transducer deforms to relax the interface stresses.

V. CONCLUDING REMARKS

Knowledge of the thermal properties of Mo/Si multilayer mirror materials is critical for determining the lifetime and optimal operating parameters for EUV optical systems. In this paper, we presented the cross-plane thermal conductivity of Mo/Si multilayer films, demonstrating an increase in thermal conductivity with increasing Mo to Si ratio. We determined the in-plane thermal conductivity of the Mo/Si multilayer stack using the 3ω technique with varying heater bridge widths, and showed it to be more than an order of magnitude greater than cross-plane thermal conductivity. These results agree with the nonequilibrium electron-phonon model of heat conduction through Mo/Si developed by Li *et al.*[32]

[1]D. G. Stearns, R. S. Rosen, and S. P. Vernon, Appl. Opt. **32**, 6952–6960 (1993).
[2]T. W. J. Barbee, S. Mrowka, and M. C. Hettrick, Appl. Opt. **24**, 883–886 (1985).
[3]E. Louis, A. E. Yakshin, T. Tsarfati, and F. Bijkerk, Prog. Surf. Sci. **86**, 255–294 (2011).
[4]J. H. Underwood and T. W. J. Barbee, Appl. Opt. **20**, 3027–3034 (1981).
[5]E. Hecht, *Optics*, 4th ed. (Addison Wesley, San Francisco, 2002).
[6]S. Bajt, J. B. Alameda, T. W. Barbee, W. M. Clift, J. A. Folta, B. Kaufmann, and E. A. Spiller, Opt. Eng. **41**, 1797–1804 (2002).
[7]K. Holloway, K. B. Do, and R. Sinclair, J. Appl. Phys. **65**, 474–480 (1989).
[8]R. S. Rosen, S. P. Vernon, D. G. Stearns, M. A. Viliardos, M. E. Kassner, and Y. Cheng, Appl. Opt. **32**, 6975–6980 (1993).
[9]E. N. Zubarev, Usp. Fiz. Nauk **54**, 473–498 (2011).
[10]G. Chen, Phys. Rev. B **57**, 14958–14973 (1998).
[11]E. N. Zubarev, V. V. Kondratenko, Y. P. Pershyn, and V. A. Sevryukova, Thin Solid Films **520**, 314–319 (2011).
[12]D. P. Gaines, R. C. Spitzer, N. M. Ceglio, M. Krumney, and G. Ulm, Appl. Opt. **32**, 6991–6998 (1993).
[13]S. Bajt, Z. R. Dai, E. J. Nelson, M. A. Wall, J. B. Alameda, N. Q. Nguyen, S. L. Baker, J. C. Robinson, J. S. Taylor, A. Aquila, and N. V. Edwards, J. Microlithogr., Microfabr., Microsyst. **5**, 023004 (2006).
[14]P.-Y. Yan, E. Spiller, and P. Mirkarimi, J. Vac. Sci. Technol. B **25**, 1859–1866 (2007).
[15]M. Oda, A. Ozawa, S. Ohki, and H. Yoshihara, Jpn. J. Appl. Phys., Part 1 **29**, 2616–2619 (1990).
[16]M. Takahashi, T. Ogawa, E. Hoshino, H. Hoko, B. T. Lee, A. Chiba, H. Yamanashi, and S. Okazaki, *in Tantalum Nitride Films for the Absorber Material of Refractive-Type EUVL Mask* (SPIE, Santa Clara, CA, USA, 2001), pp. 760–770.
[17]S. M. Rossnagel, J. Vac. Sci. Technol. B **20**, 2328–2336 (2002).
[18]E. Bozorg-Grayeli, Z. Li, M. Asheghi, G. Delgado, A. Pokrovsky, M. Panzer, D. Wack, and K. E. Goodson, Appl. Phys. Lett. **99**, 261906 (2011).
[19]Y. Wang, J. Y. Park, Y. K. Koh, and D. G. Cahill, J. Appl. Phys. **108**, 043507 (2010).
[20]T. Q. Qiu, C. P. Grigoropoulos, and C. L. Tien, Exp. Heat Transfer **6**, 231–241 (1993).
[21]D. G. Cahill, Rev. Sci. Instrum. **75**, 5119–5122 (2004).
[22]D. G. Cahill, Rev. Sci. Instrum. **61**, 802 (1990).
[23]J. Lee, J. P. Reifenberg, L. Zijian, L. Hom, M. Asheghi, K. SangBum, H. S. P. Wong, and K. E. Goodson, in *Measurement of Anisotropy in the Thermal Conductivity of Ge2Sb2Te5 Films* in 10th Annual Non-Volatile Memory Technology Symposium (NVMTS, Portland, OR, Oct 25–28, 2009), pp. 52–57.
[24]Z. Li, J. Lee, J. P. Reifenberg, M. Asheghi, R. G. D. Jeyasingh, H. P. Wong, and K. E. Goodson, IEEE Electron Device Lett. **32**, 961–963 (2011).
[25]J. Lee, Z. Li, J. P. Reifenberg, S. Lee, R. Sinclair, M. Asheghi, and K. E. Goodson, J. Appl. Phys. **109**, 084902 (2011).
[26]M. A. Panzer, M. Shandalov, J. A. Rowlette, Y. Oshima, C. Yi Wei, P. C. McIntyre, and K. E. Goodson, IEEE Electron Device Lett. **30**, 1269–1271 (2009).
[27]J. P. Reifenberg, K.-W. Chang, M. A. Panzer, S. Kim, J. A. Rowlette, M. Asheghi, H. -S. P. Wong, and K. E. Goodson, IEEE Electron Device Lett. **31**, 56–58 (2010).
[28]C. A. Paddock and G. L. Eesley, J. Appl. Phys. **60**, 285–290 (1986).
[29]A. Feldman, High Temp. - High Press. **31**, 293–298 (1999).
[30]E. Bozorg-Grayeli, J. P. Reifenberg, M. A. Panzer, J. A. Rowlette, and K. E. Goodson, IEEE Electron Device Lett. **32**, 1281–1283 (2011).

[31]J. H. Kim, A. Feldman, and D. Novotny, J. Appl. Phys. **86**, 3959–3963 (1999).
[32]Z. Li, S. Tan, E. Bozorg-Grayeli, T. Kodama, M. Asheghi, G. Delgado, M. Panzer, A. Pokrovsky, D. Wack, and K. Goodson, Nano Lett. **12**, 3121–3126 (2012).
[33]B. L. Zink, R. Pietri, and F. Hellman, Phys. Rev. Lett. **96**, 055902 (2006).
[34]G. A. Slack, *Solid State Physics* (Academic, New York, 1979), Vol. 34.
[35]T. P. Chow, D. H. Bower, R. L. Van Art, and W. Katz, J. Electrochem. Soc. **130**, 952–956 (1983).
[36]R. S. Muller, T. I. Kamins, and M. Chan, *Device Electronics for Integrated Circuits*, 3rd ed. (John Wiley & Sons, New York, NY, 2003).
[37]A. N. Christensen, J. Cryst. Growth **129**, 266–268 (1993).
[38]O. Thomas, J. P. Senateur, R. Madar, O. Laborde, and E. Rosencher, Solid State Commun. **55**, 629–632 (1985).